Journal of Metals, Materials and Minerals, 35(1), e2162, 2025

Enhanced photocatalytic reduction of Cr(VI) under visible light a magnetically separable TiO_2-Fe/Fe_3O_4 photocatalyst prepared from iron rusty waste

Khoirunisa KHOIRUNISA[1], Novianti Dwi LESTARI[1], Endang Tri WAHYUNI[1,*], and Taufik Abdillah NATSIR[1]

[1] *Department of Chemistry, Faculty of Mathematics and Natural Sciences, Universitas Gadjah Mada, Sekip Utara POB 21 BLs, Yogyakarta, 55281, Indonesia*

***Corresponding author e-mail**: endang_triw@ugm.ac.id

Received date:
20 September 2024
Revised date:
22 November 2024
Accepted date:
6 December 2024

Keywords:
Photoreduction;
TiO_2;
Doping;
Fe_3O_4;
Rusty waste

Abstract

This research deals with enhancing the visible activity and generating the magnetic property of TiO_2 by Fe doping and Fe_3O_4 impregnation respectively, using rusty iron waste as Fe source. The prepared TiO_2-Fe/Fe_3O_4 photocatalysts were characterized by SR-UV/Visible, FTIR, XRD, and SEM-EDX instruments. The resulting photocatalysts are responsive to visible light and can be separated magnetically and used for photoreduction of Cr (VI) ions. In the photoreduction of Cr(VI) over TiO_2-Fe/Fe_3O_4 photo-catalysts with various amounts of Fe dopant and alteration of Fe_3O_4 fraction, the photocatalyst mass, irradiation time, and solution pH were optimized. The research results assign that doping Fe to TiO_2 photo-catalysts can decrease the band gap energy (Eg) consequently improving its activity under visible irradiation. Furthermore, the magnetization of TiO_2-Fe allows it to be separated practically and effectively. The best detachable and the most active photocatalyst is shown by TiO_2-Fe/Fe_3O_4 having a Ti/Fe mole ratio of 1:0.05 and Fe_3O_4 fraction of 50.00%. The highest photo-reduction of Cr(VI) 10 mg·L^{-1} in 100 mL solution, 92.5%, can be achieved by applying 0.2 g of the photocatalyst mass, solution pH 3, in 90 min of reaction time under visible light.

1. Introduction

Chromium (Cr) in aqueous media exists in two stable oxidation states: Cr(III) and Cr(VI) ions. The cationic Cr(III) ions, Cr^{3+}, are less toxic and are even beneficial for mammals to increase milk production, can settle to alkaline pH, and play an essential role in glucose metabolism for humans [1]. Conversely, Cr(VI) ions form anions, CrO_4^{2-} and $Cr_2O_7^{2-}$, dissolve in the pH range of 1 to 14, are toxic even at low concentrations, potentially carcinogenic and mutagenic, and cause various adverse health effects such as allergic reactions, weakening of the immune system, kidney and liver damage, and even death [2]. Environmental pollution by Cr(VI) occurs due to wastewater disposal from industries such as metallurgy, textile, wood, paint, paper, and electroplating without proper treatment [3]. The World Health Organization (WHO) sets the maximum concentration limit for Cr(VI) in the environment at 0.05 mg·L^{-1} [4]. Given the negative consequences caused by Cr(VI) ions, wastewater treatment must be carried out to remove or decrease the concentration of Cr(VI) anions in wastewater.

Reported effective methods of handling Cr(VI) anions include photocatalytic reduction, which converts toxic Cr(VI) anions into safer Cr(III) cations. This process involves using light-induced reduction accelerated by a photocatalyst such as TiO_2 [5,6]. When TiO_2 is exposed to sunlight, it releases electrons (e^-) and forms positive radicals (h^+). Positive radicals can oxidize and degrade various organic solid compounds [7]. At the same time, the released electrons can act as a reducing agent and react with Cr(VI) ions to facilitate the reduction [8]. TiO_2 accelerates oxidation/degradation and reduction reactions and possesses qualities such as good stability, affordability, and non-toxic properties [9]. However, TiO_2 has a wide bandgap (E_g) energy of 3.2 eV (for TiO_2 anatase), which can only be activated by UV light. UV light only contains about 5% of the spectrum of sunlight, about 40% to 50% of visible light, and the rest is infrared radiation [10,11]. This limits the application of TiO_2 under sunlight.

Attempts to enhance TiO_2 activity under visible light exposure have often been made by doping transition metals, such as Fe [12,13]. Doping TiO_2 with dopant metal can generally form new bands between gaps in the TiO_2 structure so that the gaps become narrowed. Doping TiO_2 with Fe effectively decreases the E_g value corresponding to visible light energy, thereby increasing TiO_2 activity under visible light [14]. The source of the Fe dopant that has been used is in the form of expensive commercial salts such as $FeCl_3$ [15], $FeSO_4$ [16], and $K_3Fe(CN)_6$ [17]. The use of cheap dopant sources, iron rust waste, has also been reported [18]. However, an application for a reduction in Cr(VI) has never been reported.

At the end of the photocatalysis process, it is essential to separate the photocatalyst powder from the wastewater medium, often done by filtration. This separation method is considered less efficient as it is time-consuming and costly. Fast and practical separation was achieved by contacting magnetic rods on magnetic TiO_2 powder. The magnetization of TiO_2 was done by coating magnetite (Fe_3O_4), a strong magnetic material [19]. Fe_3O_4 coatings are commonly made by depositing Fe^{2+} and Fe^{3+} ions from expensive commercial salts [20].

An alternative approach involves obtaining the Fe^{3+} solution from the dissolution process of iron rust waste, making iron rust a more cost effective source of Fe^{3+} and a substitute for commercial salts.

In this research, TiO_2-Fe preparation was carried out to increase TiO_2 activity in the visible light region, with the addition of Fe_3O_4 to improve the material's magnetic properties and utilization of rust waste as a source of iron (Fe). The resulting TiO_2-Fe/Fe_3O_4 photocatalyst will be characterized with various instruments to ensure that doping has been successful. Furthermore, TiO_2-Fe/Fe_3O_4 were tested for photoreduction of Cr(VI) ions under visible light exposure. To obtain the best photoreduction conditions, optimization of solution pH, photocatalyst weight, reaction time, and initial concentration of Cr(VI) will be carried out.

2. Materials and methods

2.1 Materials

The materials used in this study were analytical grade without further purification. P25 Titanium dioxide (Degussa AG Company), ammonia solution (NH_3, 25% purity), iron(II) sulfate ($FeSO_4.7H_2O$), hydrochloric acid (HCl, 35% purity), nitric acid (HNO_3, 68% purity), potassium dichromate ($K_2Cr_2O_7$), 1,5-diphenylcarbazid ($C_{13}H_{14}N_4O$) were purchased from Merck. Distilled water was used in this work. Iron rust waste was obtained from the area around UGM Yogyakarta.

2.2 Preparation of Fe^{3+} solution from iron rust waste

The iron rust waste was mashed by mortar and pestle until it formed a powder. 0.8 g of iron rust powder was dissolved into aqua regia (HCl: HNO_3 with volume ratio 3:1) and heated at 70°C for 30 min. The brownish-yellow solution indicates the presence of Fe^{3+} ions, then diluted with distilled water.

2.3 Preparation of TiO_2 doped Fe using hydrothermal method

TiO_2-Fe photocatalyst was synthesized using the hydrothermal method. Initially, 1.303 g TiO_2 was dissolved in 50 mL Fe^{3+} solution from iron rust waste (mole ratio TiO_2:Fe = 1: 0.25). The solution was stirred with a magnetic stirrer for 3 h and sonicated for 30 min. Then, the hydrothermal process was carried out in an autoclave at 140°C for 14 h. After hydrothermal, the material was washed at neutral pH and dried at 80°C. The procedure was repeated by varying the mass of TiO_2 to obtain a variation in the TiO_2-Fe mole ratio of 1:0.25, 1:0.5, 1:0.75, and 1:1.

2.4 Preparation of TiO_2-Fe/Fe_3O_4

The magnetization process was carried out by adding 2.828 g of TiO_2-Fe material into 40 mL of 10 M NH_4OH. Then, it was stirred until homogeneous and heated to a constant temperature of 70°C. The solution was added Fe(II) and Fe(III) in a ratio of 1:2 with a Fe_3O_4 fraction of 25%, then a black precipitate was formed. The black precipitate was washed with distilled water until the pH was neutral and then dried in an oven at 80°C. The procedure was repeated by varying the mass of TiO_2-Fe to obtain a variation of the Fe_3O_4 fraction of 33.3%, 50%, 66.67%, and 75%.

2.5 Characterization of TiO_2-Fe/Fe_3O_4 photocatalyst

The photocatalyst powders were characterized by SR-UV/Visible, FTIR, XRD, and SEM-EDX. Spectrophotometer Reflectance Specular UV-Visible (SR-UV-Vis, 1700 Phamrmaspec) was used in the wavelength 200 mm to 800 nm, Fourier Transform Infrared Spectrophotometer (FTIR, Shimazu Prestige 21) was used in the wavenumber 4000 cm^{-1} to 400 cm^{-1}, X-ray diffractometer (XRD, Shimadzu 6000) was used in Cu Kα radiation λ = 0.15406 nm as the source of X-rays, operated at 40 kV, 25 mA, the angular range of 2θ = 10° to 80° and nickel as the filter), and Scanning Elektron Microscope with Energy Dispersive X-Ray Spectrometer (SEM-EDX, JEOL JSM-651OLA) with images taken from the microscope with × 3000 magnification.

2.6 Photocatalytic activity

The photocatalytic process was carried out using a closed reactor and a visible lamp (Philips TLD 18 W/54-765) as a light source (Figure 1). TiO_2-Fe and TiO_2-Fe/Fe_3O_4 photocatalytic tests were conducted to determine the optimum variations for Fe dopant and Fe_3O_4 magnetization for Cr(VI) reduction. The parameter variables tested were pH, catalyst dosage, Cr(VI) concentration, irradiation time, type of photocatalyst, and light source. Each process began with stirring in the dark for 30 min to obtain adsorption-desorption equilibrium. Then, the photocatalytic reaction was carried out by stirring under visible light. The process of separating the TiO_2-Fe/Fe_3O_4 photocatalyst from the Cr(VI) solution was attracted using an external magnet. The separated solution was complexed with 1,5-diphenylcarbazide, and the Cr(VI) concentration was measured using a wavelength of 542 nm. The reduction in Cr(VI) concentration in percentage was calculated by the following Equation:

$$Photocatalytic\ of\ Cr(VI)(\%) = \frac{Co - Ct}{Co} \times 100\% \qquad (1)$$

where Co was the initial concentration of Cr(VI) ($mg{\cdot}L^{-1}$) and Ct was the final concentration of Cr(VI) ($mg{\cdot}L^{-1}$).

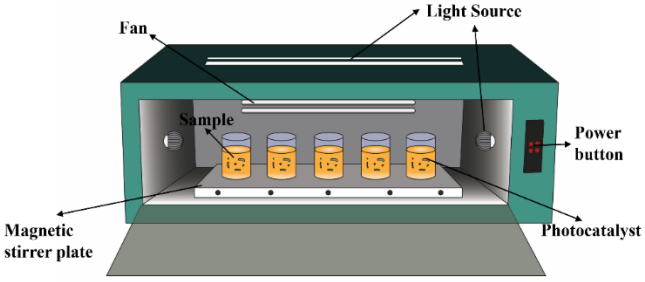

Figure 1. Schematic diagram of photocatalytic reactor.

3. Results and discussion

3.1 Analysis of iron rust waste

The XRD characterization results confirmed the type of iron oxide, as shown in the diffraction pattern in Figure 2(a). Iron rust has a semicrystalline pattern and forms diffraction peaks at 2θ: 24.17°; 49.50°; 54.23°; 62.26°; and 75.37° which shows the material characteristics of hematite (Fe_2O_3) [21]. Diffraction peaks are also formed at 2θ: 34.20°; 35.30°; 36.34°; 38.38°; and 39.38° which is a FeOOH material characteristic [22]. It indicates that rust waste has iron (Fe) content of Fe_2O_3 and FeOOH.

Figure 2(b) shows the FTIR spectra of rusty waste, confirming the presence of iron oxide. Peak absorption at wavenumber 555 cm^{-1} from the hematite compound (α-Fe_2O_3) [23]. Several peaks at wavenumbers 1635 cm^{-1}, 1126 cm^{-1}, and 447 cm^{-1} are absorption from Fe-O bonds in the compounds of β-FeOOH, γ-FeOOH, and δ-FeOOH [24,25]. The absorption peak at wavenumber 3448 cm^{-1} and 1404 cm^{-1} is the extended vibration of the O-H bond and the carbonate bond from $FeCO_3$, this compound is formed from CO_2 dissolves in water and interacts with iron oxide, the formation of this compound in iron rust can influenced by environmental [26]. Based on analysis with AAS, the percentage of Fe_2O_3 in rust waste is 81.42%.

3.2 Variation of Fe dopant (TiO_2-Fe)

TiO_2-Fe was characterized to determine changes in photocatalyst material before and after Fe doping. Based on XRD results shown in Figure 3(a), the undoped TiO_2 has a crystalline pattern with JCPDS TiO_2 anatase (00-021-1272) with several peaks appearing at 2θ: 25.28°; 36.98°; 37.93°; 48.34°; 53.99°; 54.93°; 62.69°; 70.09°; and 75.03° [27]. Diffraction patterns of TiO_2-Fe with varying levels of Fe dopants have the same peaks as TiO_2 anatase. The addition of Fe dopants decreases the peak intensity with increased Fe dopant levels indicating the successful TiO_2-Fe formed. The presence of Fe dopants interferes with the layout of the TiO_2 crystal structure and decreases the crystallinity of TiO_2.

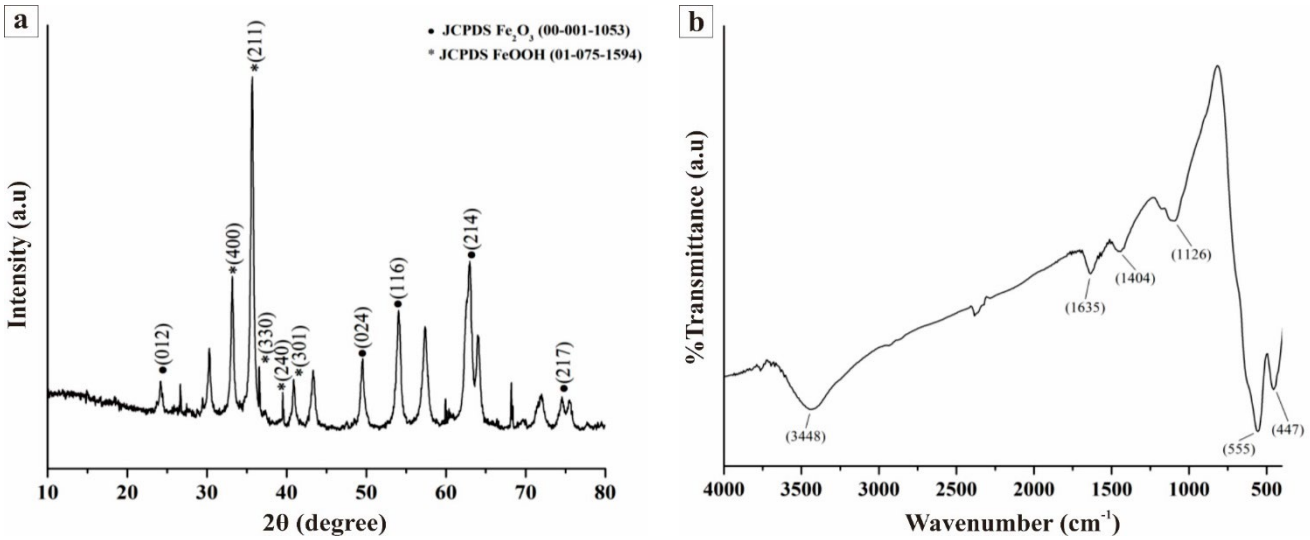

Figure 2. (a) XRD pattern and (b) FTIR spectra of waste rust.

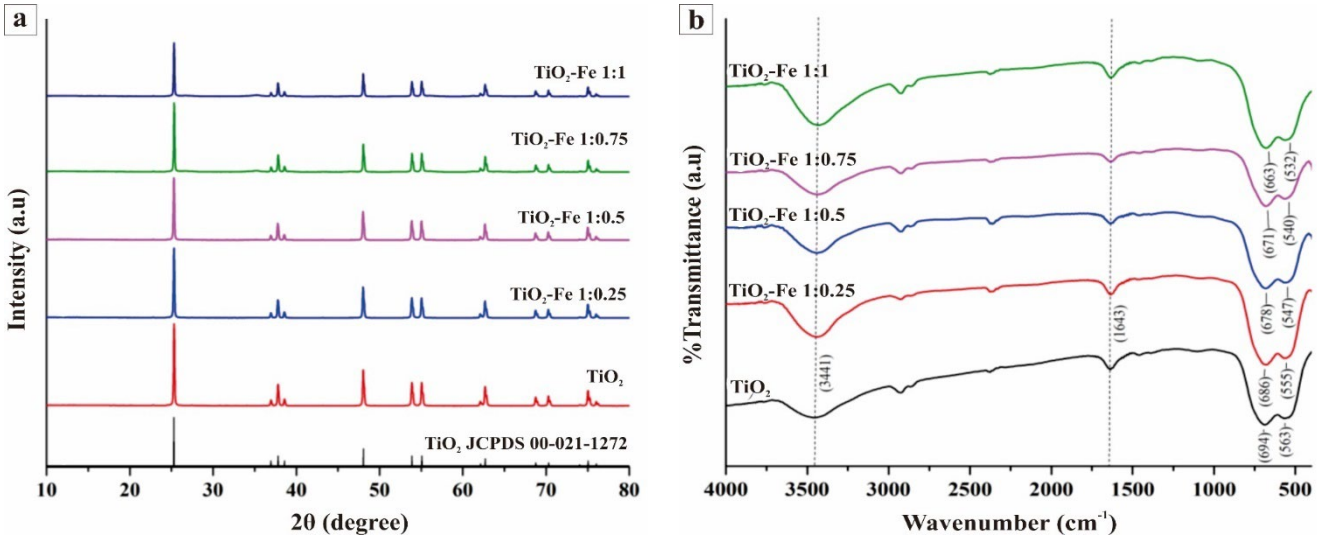

Figure 3. (a) XRD patterns and (b) FTIR spectra of TiO_2 and TiO_2-Fe.

Figure 3(b) displays the FTIR spectra, there is peak at 3441 cm^{-1} and 1643 cm^{-1} are associated with the absorption of surface O-H bonds and O-H bending vibrations from adsorbed water molecules [28]. The undoped TiO_2 has absorption at 694 cm^{-1} and 563 cm^{-1}, which is characteristic of Ti-O bonds [29]. After adding Fe, no new peaks were formed, indicating that the doping of Fe into the TiO_2 site occurred by interstitial mechanism. Fe^{3+} ions which has a partial positive charge, interacts with the oxygen atom, which has a negative charge in the TiO_2 bond. There is a shift in the absorption peak in the Ti-O-Ti bond in the wavenumber region of 500 cm^{-1} to 600 cm^{-1}; the more Fe content is added, the absorption peak shifts towards a lower wavenumber and the Ti-O-Ti bond weakens due to the interaction between the O atom and the Fe atom [30].

Fe dopant also affects the crystal size, as shown in Table 1. The TiO_2 crystal size tends to decrease as the Fe content increases to the TiO_2-Fe ratio (1:0.5). Fe doping can inhibit crystal growth, which causes the crystal size to shrink compared to undoped TiO_2. However, the TiO_2-Fe (1:0.75) has a larger crystal size, the excess dopant added causes the dopant not to dissolve properly and form excess iron aggregates in the TiO_2 matrix [30]. The decrease in crystal size confirmed by the increasing shift of the inner lattice distance also indicates that Fe^{3+} ions can enter the interstitial cavity of the TiO_2 lattice [31].The surface morphology and element content on the material surface were analyzed for TiO_2 and TiO_2-Fe (1:0.5), the most optimal mole ratio. Figure 4(a,c) displays SEM images of TiO_2 and TiO_2-Fe (1:0.5). TiO_2-Fe has a non-uniform surface compared to TiO_2 photocatalyst due to the accumulation of Fe occurs on the surface of the photocatalyst shows by clumping at several points in surface structure analyzed.

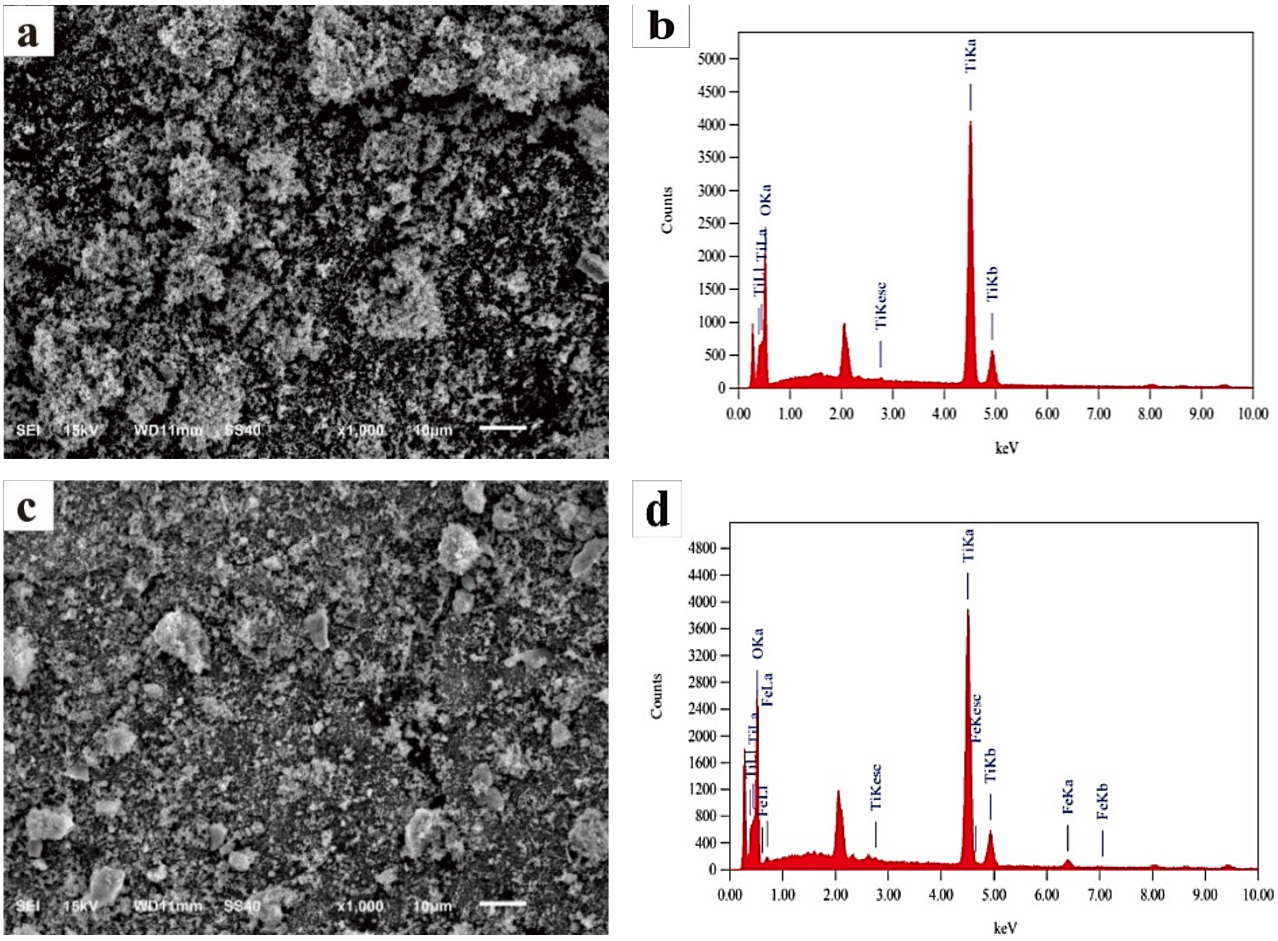

Figure 4. SEM images of (a) TiO_2, (c) TiO_2-Fe 1:0.5; EDX spectrum of (b) TiO_2, (d) TiO_2-Fe 1:0.5.

Table 1. The crystallite size of TiO_2 and TiO_2-Fe.

Material	2θ (101) (°)	d (101) (Å)	D (nm)
TiO_2	25.313	3.516	85.083
TiO_2-Fe 1:0.25	25.298	3.518	85.080
TiO_2-Fe 1:0.5	25.284	3.520	85.078
TiO_2-Fe 1:0.75	25.322	3.514	85.084
TiO_2-Fe 1:1	25.306	3.517	85.082

The EDX spectrum is also shown in Figure 4(b,d) where Ti and O element peaks were observed in the TiO_2 photocatalyst. After Fe doping, a new peak appeared: the Fe element peak that indicates the Fe doping process on the TiO_2 photocatalyst has been successful. Adding Fe can also reduce the percentage of the Ti element because the interaction between Fe atoms doped in the TiO_2 structure causes a redistribution of atoms in the crystal matrix and changes the proportion of Ti atoms in the material. The levels of each element are presented in Table 2.

The SR-UV spectrum shows that the higher the amount of dopant added, the more significant the shift towards visible light wavelengths (Figure 5(a)). Absorption edges correspond to the transfer of electrons from the valence band to the conduction band. In the Fe^{3+} ion, the 3d orbital is half-filled, when doped with TiO_2, the empty state is at the bottom of the conduction band while the filled t_{2g} is at the top of the valence band. The TiO_2-Fe absorption band shows a wider band than the TiO_2 absorption band which confirms that Fe^{3+} doping on TiO_2 induces electronic states (Fe^{4+} and Fe^{2+}) in the TiO_2 band gap.

Band gap energy (E_g) was calculated using the Tauc plot method and displayed in Figure 5(b). It shows that the addition of Fe^{3+} dopant to the TiO_2 crystal lattice results in a decrease in the E_g value to the TiO_2-Fe variation (1:0.5). The reduction in the E_g value occurs due to the formation of a new band by inserting a new energy level from the Fe^{3+} dopant into the TiO_2 band gap. The higher the Fe^{3+} concentration, the narrower the valence and conduction band gaps in TiO_2 and the smaller the band gap energy formed. However, when the dopant level increases (1:0.75 and 1:1), the energy in the bandgap increases due to the Fe^{3+} dopant concentration that exceeds the optimal dopant concentration will form large deposits covering the photocatalyst's surface, thereby reducing the effective surface area for absorbing light [32]. Cr(VI) photoreduction results in Figure 5(c) show that the Fe-doped TiO_2 photocatalyst material provides higher photoreduction activity than undoped TiO_2. The doping process with Fe reduces the E_g of TiO_2 and shifts its absorption band to the visible light wavelength region so that the Cr(VI) photoreduction process works effectively in visible light and the TiO_2:Fe variation (1:0.5) has the highest photoreduction percentage. The high concentrations of Fe dopant lead to the saturated TiO_2 crystal lattice with Fe^{3+} ions and competition occurs with the redox reactions on the photocatalyst surface [33].

3.3 Variation magnetization of Fe_3O_4 (TiO_2-Fe/Fe_3O_4)

Characterization was carried out after adding various variations of Fe_3O_4 to the TiO_2-Fe photocatalyst. The diffraction pattern of Fe_3O_4 material is shown in Figure 6(a), which has peak at 2θ: 30.09°, 35.42°, 43.05°; 53.40°, 56.94°; and 62.52°. This diffraction pattern corresponds to the cubic plane crystal structure of Fe_3O_4 with JCPDS 00-019-0629 [34]. After adding Fe_3O_4, a diffraction pattern of Fe_3O_4 appears; the higher the Fe_3O_4 content, the higher the peak intensity [35]. Figure 6(a) shows an anatase peak, such as TiO_2-Fe, before adding Fe_3O_4. The intensity of the anatase peak decreased with increasing Fe_3O_4 levels due to structural changes as evidenced by FTIR data in the form of overlapping peaks forming Ti-O-Fe bonds and a decrease in the amount of TiO_2-Fe in the sample in Table 3. Adding Fe_3O_4 tends to reduce the crystal size because the presence of Fe_3O_4 can inhibit crystal growth in the TiO_2-Fe mixture. Increasing the levels of Fe_3O_4 added did not change the crystal size significantly. When the Fe_3O_4 particles interact with TiO_2-Fe, it causes deformation or changes in the TiO_2-Fe lattice structure [49]. This deformation can cause a reduction in the distance between planes and shrinkage or compaction of the TiO_2-Fe crystal structure [36].

The FTIR results graph in Figure 6(b) shows the absorption characteristics of Fe_3O_4 material. Absorption peaks at wavenumbers 3441 cm^{-1} and 1643 cm^{-1} indicate the O-H stretching and bending vibrations of H_2O molecules, and vibrational extension of Fe-O bonds appears at wavenumber 601 cm^{-1} [37]. The FTIR spectra of the TiO_2-Fe/Fe_3O_4 material with various magnetization concentrations show peaks at wavenumbers 676 cm^{-1} and 686 cm^{-1}, indicating the increased vibration of the Ti-O bond. With higher TiO_2-Fe content, the vibration frequency shifts to a higher wavenumber, means the stronger the Ti-O bond. Increasing the percentage of Fe_3O_4 addition results in a widening of the Ti-O peak in the frequency region of 500 cm^{-1} to 700 cm^{-1} due to the overlap of the peaks of the Ti-O bond and the Fe-O bond, which confirms the success of the magnetization process of Fe_3O_4 with TiO_2-Fe [38].

Based on the SEM image in Figure 7(a), the morphology of the Fe_3O_4 material is in the form of large aggregates. This aggregation occurs due to the magnetic properties of Fe_3O_4, which causes the particle's tendency to group and interact with the charged Fe_3O_4 particles [39]. Figure 7(b-f) shows the morphology of the TiO_2-Fe/Fe_3O_4 material. The higher the Fe_3O_4 content added, the surface morphology of the material forms large lumps similar to the surface of Fe_3O_4. The addition of Fe_3O_4 causes agglomeration by van der Waals forces and magnetic dipoles in iron magnetic particles, as well as a higher band gap in TiO_2 particles [40].

The EDX spectra are shown in Figure 7; the Fe_3O_4 material has characteristic peaks for the elements Fe and O. In the TiO_2-Fe/Fe_3O_4 material, peaks indicate the presence of the elements Ti, Fe, and O. The EDX spectrum shows the absence of other elements; confirms the absence of other impurities in the structure of the synthesized TiO_2-Fe/Fe_3O_4. Table 4 confirmed the success of the synthesis process of adding Fe_3O_4 to the TiO_2-Fe material.

Table 2. The elements composition of TiO_2 and TiO_2-Fe from EDX analysis.

Element	Mass percentage (%)	
	TiO_2	TiO_2-Fe
Ti	26.19	22.39
O	73.81	76.36
Fe	-	1.25

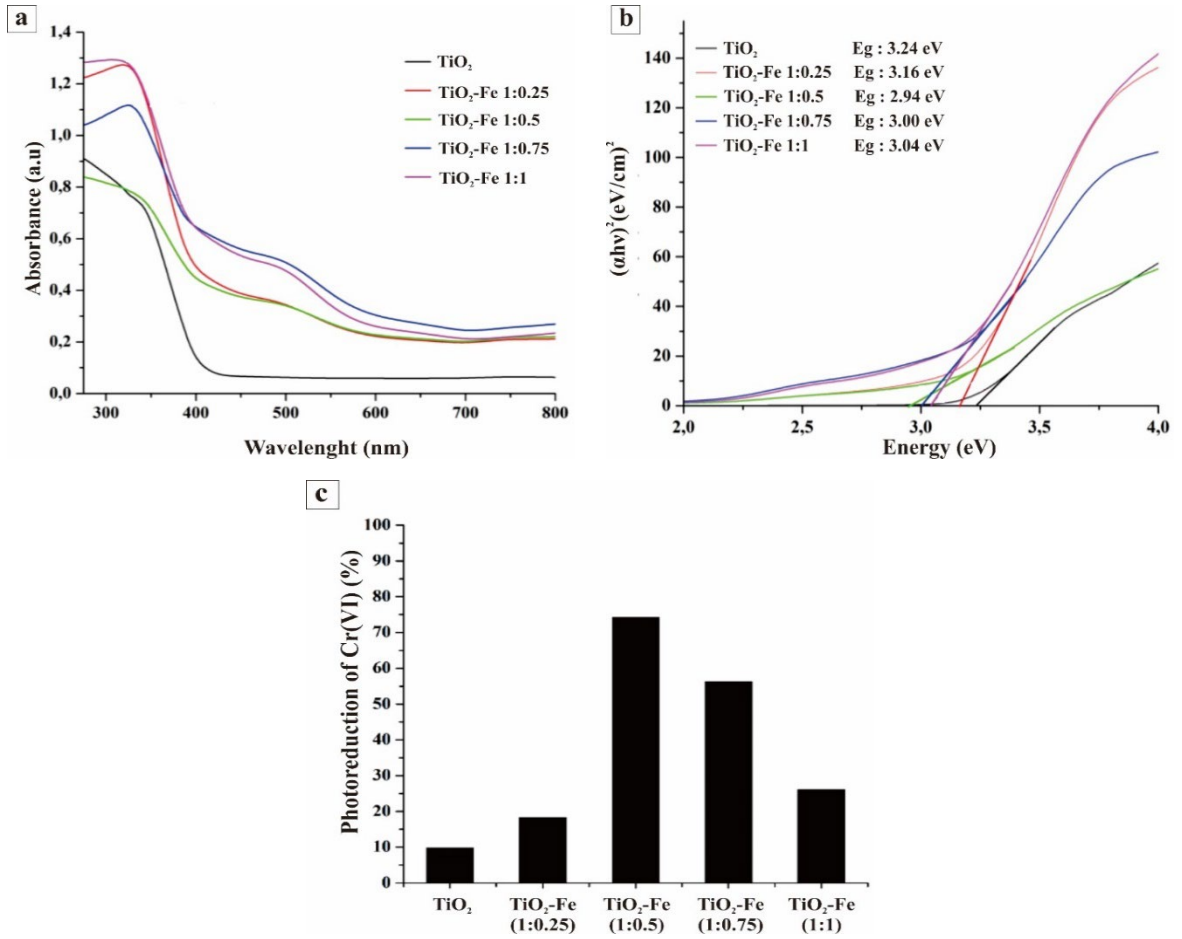

Figure 5. (a) SRUV-Vis spectrum, (b) Tauc's plot of TiO_2 and TiO_2-Fe, (c) effectiveness of TiO_2 and TiO_2-Fe on photoreduction of Cr(VI).

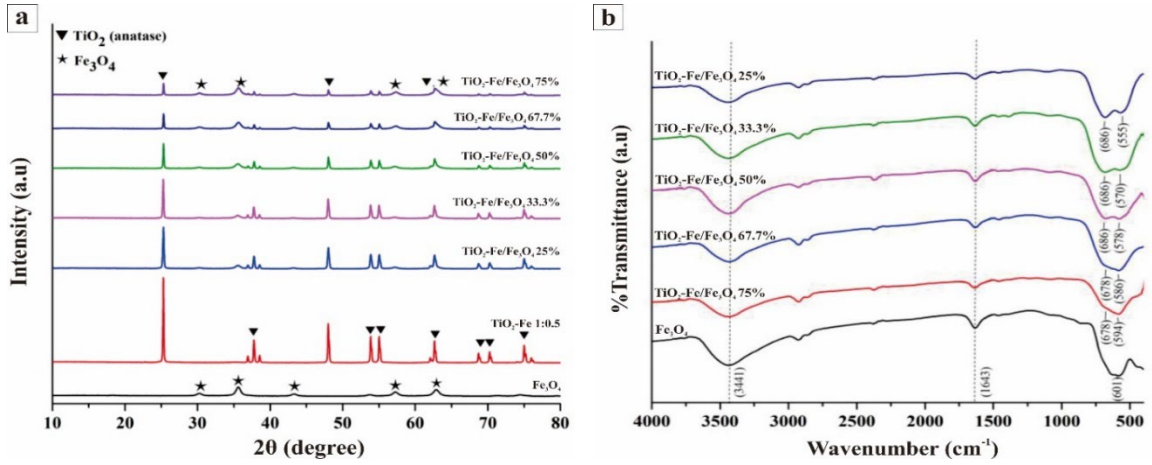

Figure 6. (a) XRD patterns and (b) FTIR spectra of TiO_2-Fe/Fe_3O_4

Table 3. The average crystallite sizes of Fe_3O_4 and TiO_2-Fe/Fe_3O_4.

Material	2θ (°)	d (Å)	D (nm)
Fe_3O_4	35.635	2.517	71.481
TiO_2-Fe 1:0.5	25.284	3.520	83.512
TiO_2-Fe/Fe_3O_4 25%	25.299	3.518	65.628
TiO_2-Fe/Fe_3O_4 33.3%	25.270	3.522	76.297
TiO_2-Fe/Fe_3O_4 50%	25.311	3.516	78.878
TiO_2-Fe/Fe_3O_4 67.7%	25.319	3.514	84.605
TiO_2-Fe/Fe_3O_4 75%	25.310	3.516	78.903

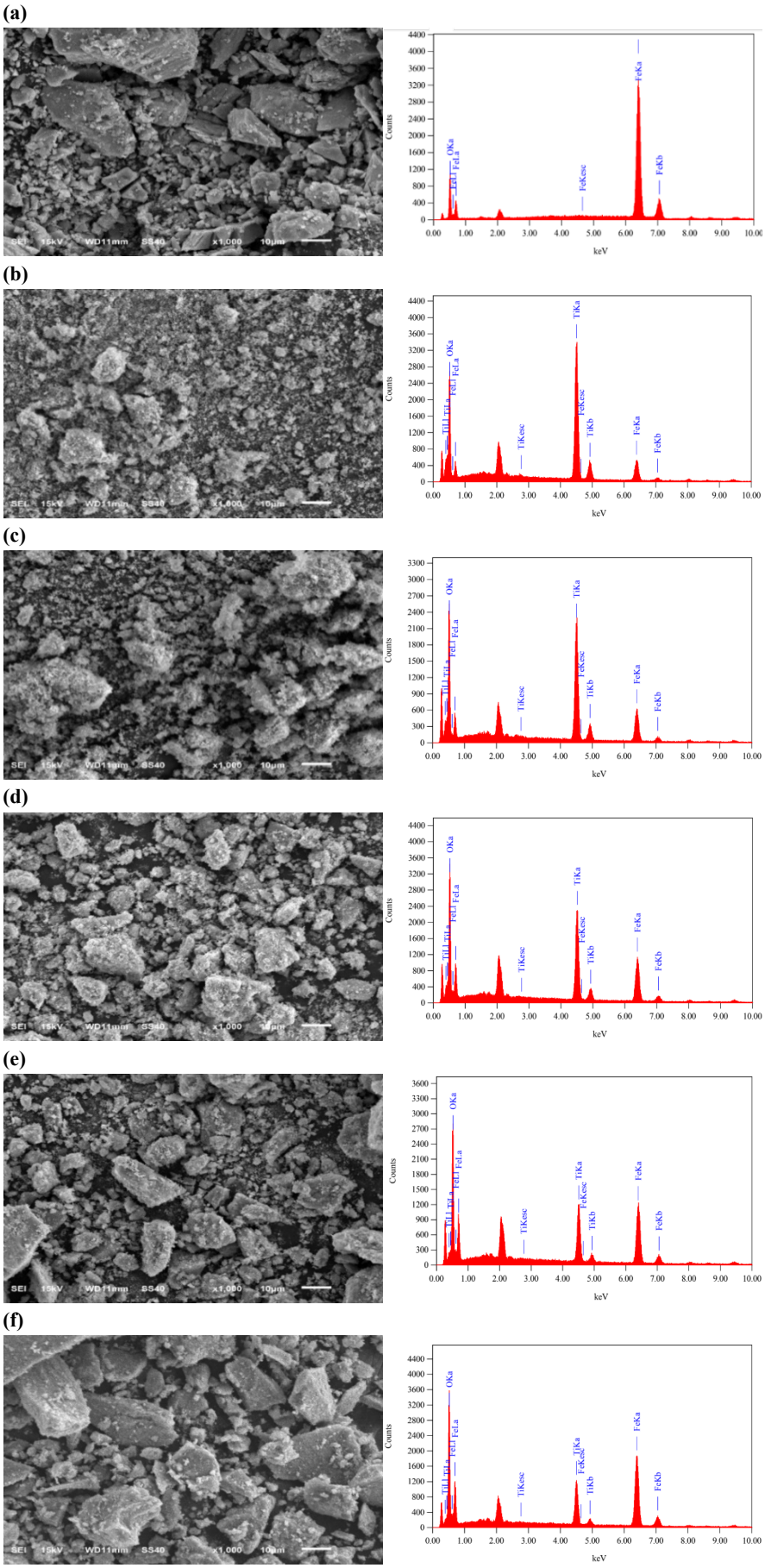

Figure 7. SEM images and EDX spectrum of (a) Fe_3O_4 and TiO_2-Fe/Fe_3O_4 (b) 25%, (c) 33.3%, (d) 50%, (e) 67.7%, (f) 75%.

Table 4. The elements composition of Fe_3O_4 and TiO_2-Fe/Fe_3O_4 from EDX analysis.

Element	Mass percentage (%)					
	Fe_3O_4	TiO_2-Fe/Fe_3O_4 (1:0.3)	TiO_2-Fe/Fe_3O_4 (1:0.5)	TiO_2-Fe/Fe_3O_4 (1:1)	TiO_2-Fe/Fe_3O_4 (1:2)	TiO_2-Fe/Fe_3O_4 (1:3)
Ti	-	20.98	16.67	13.98	9.94	8.28
O	22.09	72.50	74.15	71.93	68.57	63.57
Fe	77.91	6.52	9.18	14.09	21.49	28.15

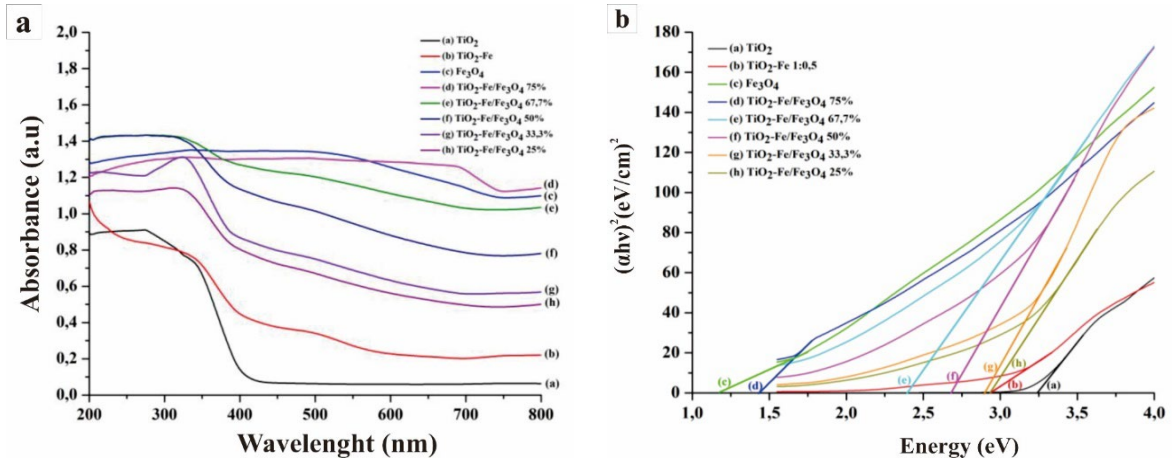

Figure 8. (a) SRUV-Vis spectrum, and (b) Tauc's plot of TiO_2, TiO_2-Fe, and TiO_2-Fe/Fe_3O_4.

The SR-UV spectra of TiO_2, TiO_2-Fe, and TiO_2-Fe/Fe_3O_4 materials are shown in Figure 8(a). Fe_3O_4 has strong absorption in the visible light region. The spectrum tends to be straight due to the transfer of electrons from the valence to the conduction band at a very short distance. The energy required is small, so the absorption distribution becomes relatively low, even in certain spectral areas. The magnetization process expands the light absorption range of TiO_2-Fe in visible light; the higher the Fe_3O_4 content, the more the additional wavelength reaches the visible light area. The increase in absorption is caused by a charge transfer transition between the iron oxide nanoparticle electrons and the conduction band (or valence band) of TiO_2. The Tauc plot equation measures the E_g of the TiO_2-Fe/Fe_3O_4 photocatalyst and the result is displayed in Figure 8(b). Increasing the added levels of Fe_3O_4 causes the band gap energy value to become smaller due to the inclusion of iron oxide (Fe_3O_4) into the TiO_2 structure [37,41].

3.4 Photocatalytic reduction of Cr(VI) using TiO_2-Fe/Fe_3O_4 photocatalyst

3.4.1 Photocatalytic activity

Testing the effect of the Fe_3O_4 content added to the TiO_2-Fe/Fe_3O_4 photocatalyst aims to determine the optimum Fe_3O_4 that can produce maximum effectiveness in the Cr(VI) photoreduction process and the magnetization separation process. Based on Figure 9, there was a significant increase in the effectiveness of Cr(VI) photoreduction. The addition of Fe_3O_4 content increases the effectiveness of Cr(VI) photoreduction due to its support in the adsorption process. More over, higher Fe_3O_4 content decreases the Eg value of TiO_2-Fe/Fe_3O_4 and enhancing the absorption of visible light. However, excessive Fe_3O_4 levels reduce Cr(VI) photoreduction activity by covering the TiO_2-Fe photocatalyst surface, hindering light absorption and suboptimal electron production. Subsequently, the photocatalyst process, aided by sunlight, facilitates the reduction of Cr(VI) to Cr(III).

The ability to separate the photocatalyst from the Cr(VI) photoreduction solution was tested using a magnetic bar, as shown in Figure 10. Qualitatively, the results of separating filtrate with higher Fe_3O_4 content tend to be clearer because its magnetic properties are stronger. On the other hand, a lower Fe_3O_4 content results in weaker the magnetic properties and increase the turbidity. Quantitative testing using a turbidimeter confirmed these findings. Figure 10 illustrates that as the Fe_3O_4 content increases, the turbidity value decreases, leading to a clearer filtrate. The optimal photocatalyst content was found to TiO_2-Fe/Fe_3O_4 variation of 50%, as it demonstrated good Cr(VI) photoreduction activity and effective filtrate separation. As a result, the TiO_2-Fe/Fe_3O_4 photocatalyst at 50% is used in this research for further optimization.

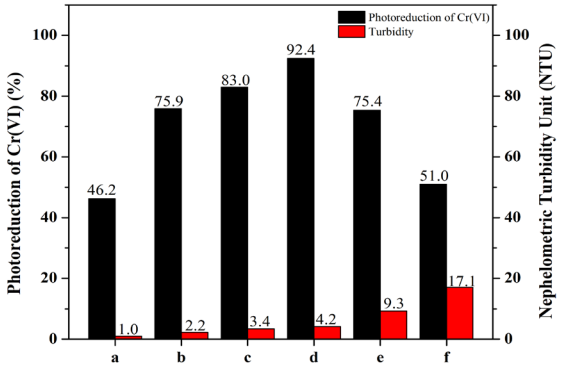

Figure 9. Cr(VI) photoreduction ability and turbidity of the separation filtrate with magnets for (a) Fe_3O_4 and TiO_2-Fe/Fe_3O_4 (b) 25%, (c) 33.3%, (d) 50%, (e) 67.7%, and (f) 75%.

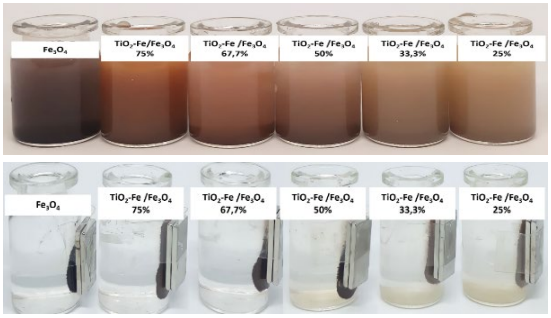

Figure 10. Magnetic separation of Fe_3O_4 and TiO_2-Fe/Fe_3O_4 after photoreduction Cr(VI).

Figure 11(a) shows the maximum photoreduction Cr(VI) effectiveness at pH 3. The TiO_2-Fe/Fe_3O_4 photocatalyst has a PZC value of 6.8, indicating that the pH of the surface charge of the photocatalyst is neutral. When the pH is 3, the photocatalyst becomes positively charged, leading to adsorption processes and electrostatic interactions between the photocatalyst surface and Cr(VI) ions. The surface charge of the photocatalyst can be either positive or negative depending on the pH of the solution, as determined by the Equation:

$$pH < pHPZC : TiOH + H^+ \rightarrow TiOH_2^+ \quad (2)$$

$$pH > pHPZC : TiOH + OH^- \rightarrow TiO^- + H_2O \quad (3)$$

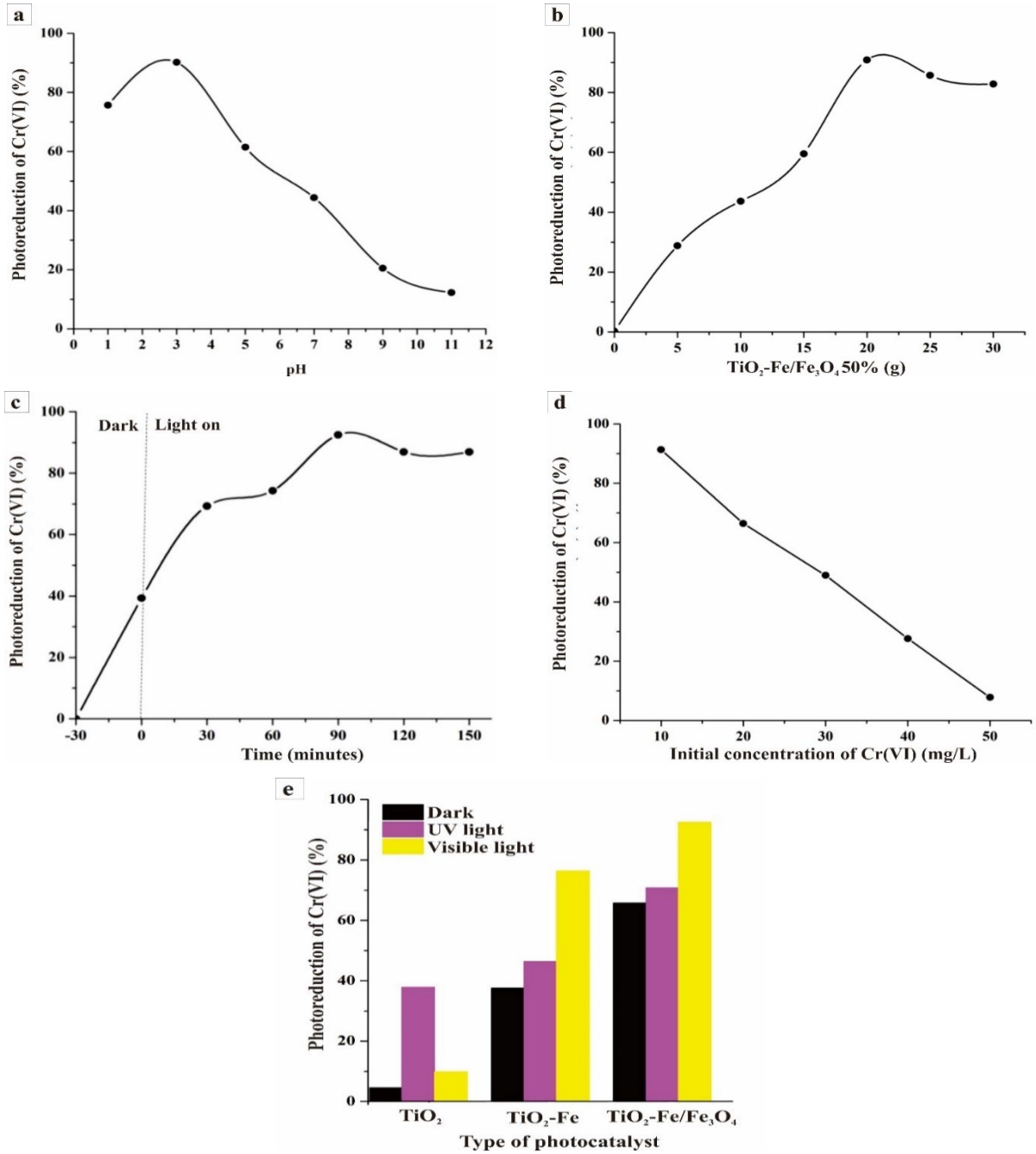

Figure 11. Influence of (a) pH, (b) dosage photocatalyst, (c) irradiation time, (d) initial concentration of Cr(VI), (f) light source on photoreduction Cr(VI) using TiO_2-Fe/Fe_3O_4 50%.

At pH 1, a highly acidic environment hinders photoreduction due to increased production of hydrogen ions (H^+), which can interact with the surface of TiOH (hydrated TiO_2) to form $TiOH_2^+$ (Equation (1)) and inhibits the release of electrons on the photocatalyst [7]. As the pH increases within the acidic range, electron release improves. However, at pH 5 and 7, the percentage of photoreduction Cr(VI) decreases due to fewer electronic interactions. Under alkaline solution conditions (pH 9 and pH 11), the surface of the photocatalyst is negatively charged, and there is a repulsive force between the surface charge of the photocatalyst and Cr(VI) ions, where Cr(VI) in alkaline solution exists in the form of CrO_4^{2-}, which reduces its ability to reduce Cr(VI). High pH conditions can create a negative surface on TiO_2 and form TiO^- which can inhibit electron release (Equation (2)) [7], leading to the formation of $Cr(OH)_3$ solids which cover the active surface of the photocatalyst, and reducing absorption of chromate ions [42].

The impact of photocatalyst dosage on the effectiveness of Cr(VI) photoreduction is illustrated in Figure 11(b). As the photocatalyst dosage increases from 2 mg to 20 mg. the efficiency of Cr(VI) photoreduction also increases. It attributed to the larger surface area for the photocatalytic reaction and enhanced light absorption as a result of the greater dosage [43]. Meanwhile, when the dosage exceeds 20 mg, the effectiveness of Cr(VI) photoreduction decreases. The excess dosage of the photocatalyst causes turbidity and light reflection in the solution. Consequently, the interaction between light and the photocatalyst is reduced. Resulting in lowered photoreduction of Cr(VI) [44].

The impact of photocatalyst dosage on the effectiveness of Cr(VI) photoreduction is illustrated in Figure 11(b). As the photocatalyst dosage increases from 2 mg to 20 mg. the efficiency of Cr(VI) photoreduction also increases. It attributed to the larger surface area for the photocatalytic reaction and enhanced light absorption as a result of the greater dosage [43]. Meanwhile, when the dosage exceeds 20 mg, the effectiveness of Cr(VI) photoreduction decreases. The excess dosage of the photocatalyst causes turbidity and light reflection in the solution. Consequently, the interaction between light and the photocatalyst is reduced. Resulting in lowered photoreduction of Cr(VI) [44]. The effect of irradiation time is presented in Figure 11(c). The initial irradiation stage is carried out in dark conditions for 30 min to assess adsorption capability and ability to maintain the adsorption-desorption balance of the photocatalyst [45]. The longer the irradiation time, the higher the percentage of photoreduction Cr(VI). The longer irradiation time increases the contact between light and the photocatalyst, resulting in a greater number of electrons [46]. Longer irradiation time enhances the interaction between electrons and Cr(VI) ions, increasing the effectiveness of Cr(VI) photoreduction. The photo-reduction time of Cr(VI) reaches its maximum level at 90 min of light. When the irradiation time is more than 90 min, there is a decrease in the percentage of photoreduction Cr(VI) because the active side of the photocatalyst has been saturated to absorb photon energy. Hence, the electrons produced are not optimal. Irradiation times longer than the optimum time can also produce vast quantities of product that prevent contact between reacting substances. As a result, the performance of the photocatalyst is inhibited to release more electrons so that it cannot increase the photoreduction of Cr(VI) [7].

The influence of photocatalyst type was investigated to assess the effect of TiO_2 photocatalyst without and with Fe doping, and the inclusion of Fe_3O_4 magnetic material on Cr(VI) photoreduction under varied light circumstances. Figure 11(e) shows the photocatalyst efficiency of TiO_2, TiO_2-Fe, and TiO_2-Fe/Fe_3O_4 respond similarly to dark conditions, UV light, and visible light. The photocatalyst effectiveness in dark conditions rises with the addition of Fe dopant and Fe_3O_4 due to Fe dopant increasing surface porosity and adsorption capacity, also Fe_3O_4 is an adsorbent with high adsorption efficiency [19]. Under UV light irradiation, adding Fe and Fe_3O_4 improves the photocatalyst effectiveness since these two substances can reduce the recombination rate [37]. When exposed to visible light, the effectiveness of the photocatalyst increases due to the inclusion of Fe and Fe_3O_4 shifting the wavelength from UV to visible light, allowing the photocatalyst to absorb light optimally [37].

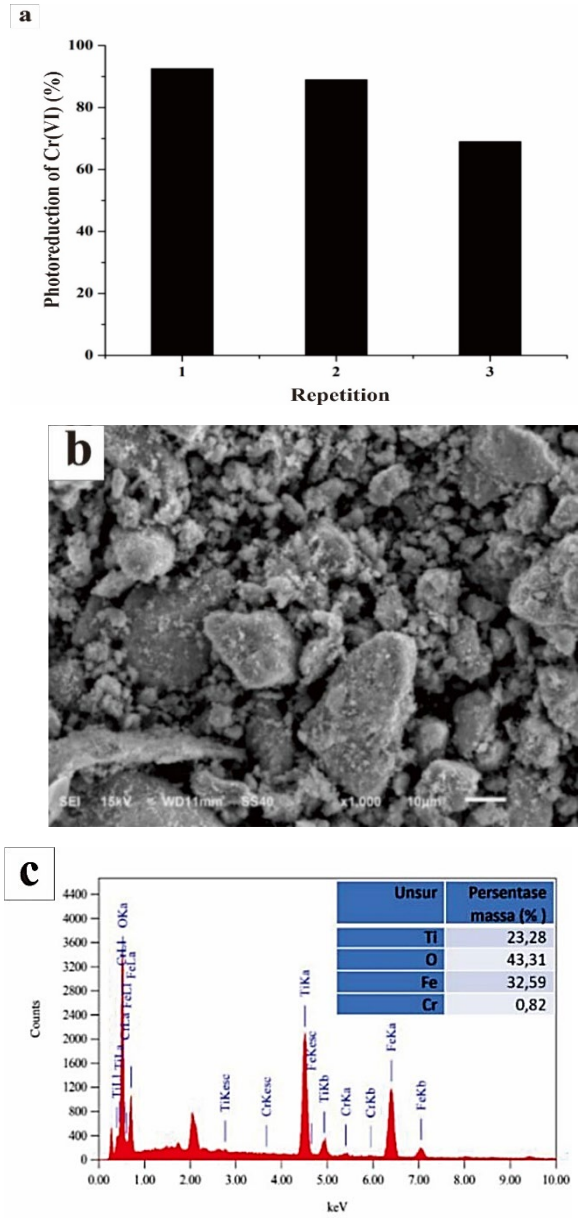

Figure 12. (a) Reusability tests of Cr(VI), (b) SEM image, and (c) EDX spectrum of TiO_2-Fe/Fe_3O_4 after 3 runs.

3.4.2 Reusability test

The photocatalyst reuse test aims to evaluate the stability of the photocatalytic activity of TiO_2-Fe/Fe_3O_4 photocatalysts. Figure 12(a) displays that the first and second uses of TiO_2-Fe/Fe_3O_4 photocatalysts demonstrate effective and stable Cr(VI) photoreduction. However, during the third use, photocatalysts experienced a significant decrease in Cr(VI) photoreduction due to the disruption of the photocatalyst's performance caused by the presence of Cr(III) ions from the absorbed photoreduction process. These ions lead to the formation of $Cr(OH)_3$ deposits on the surface of the photocatalyst, blocking photon light absorption and limiting the performance of its active sites. Additionally, it can also promote the recombination of electron charge (e^-) and hole (h^+) [47]. The results of SEM in Figure 12(b) show that the particle size of the TiO_2-Fe/Fe_3O_4 photocatalyst appears larger due to the accumulation of $Cr(OH)_3$ on its surface after the Cr(VI) photoreduction process. This is further supported by the EDX results in Figure 12(c), indicating 0.82% mass percentage of Cr, confirming the presence of Cr solids on the surface of the photocatalyst.

4. Conclusions

Doping Fe from iron rusty waste and impregnation of Fe_3O_4 to TiO_2 photocatalyst was successfully synthesized, adding Fe dopant (1:0.5) can shift the photocatalyst absorption to the visible light area and 50% Fe_3O_4 makes the photocatalyst separation process easier. The highest Cr(VI) photoreduction, 92.5%, is achieved by applying 10 $mg \cdot L^{-1}$ Cr(VI) at pH 3 with 0.2 g TiO_2-Fe/Fe_3O_4 in 90 min under visible light. After three uses, the photocatalyst still exhibited good results, showing potential for addressing the environmental issue of Cr(VI) waste.

Credit author statement

Khoirunisa: Methodology, Writing-Original draft, N. D. Lestari: Software, Writing-Review and Editing, E. T. Wahyuni: Conceptualization, Supervision, T.A. Natsir : Supervision, Writing-Review and Editing.

Conflict of Interest Statement

The authors declare that the research was conducted in the absence of any commercial or financial relationships that could be construed as a potential conflict of interest

Acknowledgment

The author would like to acknowledge the Faculty of Mathematics and Natural Sciences, Universitas Gadjah Mada for the financial support through a Lecturer Research Grant Number 53/UN1/FMIPA.1.3/KP/PT.01.03/2023.

References

[1] J. Zhang, S. Lin, M. Han, Q. Su, L. Xia, and Z. Hui, "Adsorption properties of magnetic magnetite nanoparticle for coexistent Cr(VI) and Cu(II) in mixed solution," *Water (Switzerland)*, vol. 12, no. 2, pp. 1-13, 2020.

[2] H. Karimi-Maleh, A. Ayati, S. Ghanbari, Y. Orooji, B. Tanhaei, F. Karimi, M. Alizadeh, J. Rouhi, L. Fu, and M. Sillanpaa, "Recent advances in removal techniques of Cr(VI) toxic ion from aqueous solution: A comprehensive review," *Journal of Molecular Liquids*, vol. 329, p. 115062, 2021.

[3] E. Prabakaran, and K. Pillay, "Self-assembled silver nanoparticles decorated on exfoliated graphitic carbon nitride/carbon sphere nanocomposites as a novel catalyst for catalytic reduction of Cr(VI) to Cr(III) from wastewater and reuse for photocatalytic applications," *ACS Omega*, vol. 6, no. 51, pp. 35221-35243, 2021.

[4] J. Ding, L. Pu, Y. Wang, B. Wu, A. Yu, X. Zhang, C. Pan, Q. Zhang, and G. Gao, "Adsorption and reduction of Cr(VI) together with Cr(III) sequestration by polyaniline confined in pores of polystyrene beads," *Environmental Science and Technology*, vol. 52, no. 21, pp. 12602-12611, 2018.

[5] R. Acharya, B. Naik, and K. Parida, "Cr(VI) remediation from aqueous environment through modified-TiO_2-mediated photocatalytic reduction," *Beilstein Journal of Nanotechnology*, vol. 9, no. 1, pp. 1448-1470, 2018.

[6] R. Djellabi, P. Su, E. A. Elimian, V. Poliukhova, S. Nouacer, I. A. Abdelhafeez, N. Abderrahim, D. Aboagye, V. V. Andhalkar, W. Nabgan, S. Rtimi, and S. Contreras, "Advances in photocatalytic reduction of hexavalent chromium: From fundamental concepts to materials design and technology challenges," *Journal of Water Process Engineering*, vol. 50, p. 103301, 2022.

[7] E. T. Wahyuni, and N. H. Aprilita, "Photoreduction processes over TiO_2 photocatalyst," *Photocatalysts - Applications and Attributes*, p. 80914, 2019.

[8] R. Djellabi, F. M. Ghorab, S. Nouacer, A. Smara, and O. Khireddine, "Cr(VI) photocatalytic reduction under sunlight followed by Cr(III) extraction from TiO_2 surface," *Materials Letters*, vol. 176, pp. 106-109, 2016.

[9] Z. Wu, X. Liu, C. Yu, F. Li, W. Zhou, and L. Wei, "Construct interesting CuS/TiO_2 architectures for effective removal of Cr(VI) in simulated wastewater via the strong synergistic adsorption and photocatalytic process," *Science of the Total Environment*, vol. 796, p. 148941, 2021.

[10] Z. Chen, J. Ma, K. Yang, S. Feng, W. Tan, Y. Tao, H. Mao, and Y. Kong, "Preparation of S-doped TiO_2-three dimensional graphene aerogels as a highly efficient photocatalyst," *Synthetic Metals*, vol. 231, pp. 51-57, 2017.

[11] M. Hamadanian, A. Reisi-Vanani, P. Razi, S. Hoseinifard, and V. Jabbari, "Photodeposition-assisted synthesis of novel nanoparticulate In, S-codoped TiO_2 powders with high visible light-driven photocatalytic activity," *Applied Surface Science*, vol. 285, no. Part B, pp. 121-129, 2013.

[12] Y. Li, P. Zhang, J. Zhang, H. Zhang, T. Ai, Z. Zhao, Y. Liu, Z. Pu, "Photocatalytic performance of Fe doped TiO_2 on the surface of carbon fiber," *Optical Materials*, vol. 133, no. 13 p. 112970, 2022.

[13] T. Jiang, J. Chai, Y. Wang, Q. Du, J. Shi, and Z. Xu, "Enhanced photocatalytic reduction of Cr(VI) from aqueous solution using Fe0/TiO_2-based polymeric nanocomposites," *Environmental*

Science and Pollution Research, vol. 30, no. 51, pp. 110312-110323, 2023.

[14] I. Mironyuk, N. Danyliuk, T. Tatarchuk, I. Mykytyn, and V. Kotsyubynsky, "Photocatalytic degradation of Congo red dye using Fe-doped TiO_2 nanocatalysts," *Physics and Chemistry of Solid State*, vol. 22, no. 4, pp. 697-710, 2021.

[15] K. Vijayalakshmi, and S. D. Jereil, "Influence of Fe catalytic doping on the properties of TiO_2 nanoparticles synthesized by microwave method," *Journal of Materials Science: Materials in Electronics*, vol. 25, no. 11, pp. 5089-5094, 2014.

[16] S. C. Xu, S. S. Pan, Y. Xu, Y. Y. Luo, Y. X. Zhang, and G. H. Li, "Efficient removal of Cr(VI) from wastewater under sunlight by Fe(II)-doped TiO_2 spherical shell," *Journal of Hazardous Materials*, vol. 283, pp. 7-13, 2015.

[17] J. C. Te Lin, M. D. G. de Luna, M. J. N. Gotostos, and M. C. Lu, "Effects of doping amounts of potassium ferricyanide with titanium dioxide and calcination durations on visible-light degradation of pharmaceuticals," *Environmental Science and Pollution Research*, vol. 23, no. 22, pp. 22721-22733, 2016.

[18] E. T. Wahyuni, N. D. Lestari, I. R. Cinjana, S. Annur, T. A. Natsir, and M. Mudasir, "Doping TiO_2 with Fe from iron rusty waste for enhancing its activity under visible light in the Congo red dye photodegradation," *Journal of Engineering and Applied Science*, vol. 70, no. 1, pp. 1-14, 2023.

[19] S. Al-Salihi, M. Bayati, A. M. Jasim, M. M. Fidalgo, and Y. Xing, "Magnetic mesoporous TiO_2/Fe_3O_4 nanocomposite adsorbent for removal of sulfamethazine from water," *Environmental Advances*, vol. 9, p. 100283, 2022.

[20] M. M. Ba-Abbad, A. Benamour, D. Ewis, A. W. Mohammad, and E. Mahmoudi, "Synthesis of Fe_3O_4 nanoparticles with different shapes through a co-precipitation method and their application," *Jom*, vol. 74, no. 9, pp. 3531-3539, 2022.

[21] M. H. Lee, J. H. Park, H. S. Han, H. J. Song, I. S. Cho, J. H. Noh, and K. S. Hong, "Nanostructured Ti-doped hematite (α-Fe_2O_3) photoanodes for efficient photoelectrochemical water oxidation," *International Journal of Hydrogen Energy*, vol. 39, no. 30, pp. 17501-17507, 2014.

[22] J. Xiao, A. M. Oliveira, L. Wang, Y. Zhao, T. Wang, J. Wang, B. P. Setzler, and Y. Yan, "Water-fed hydroxide exchange membrane electrolyzer enabled by a fluoride-incorporated nickel−iron oxyhydroxide oxygen evolution electrode," *ACS Catalysis*, vol. 11, no. 1, pp. 264-270, 2020.

[23] M. Shaban, M. Binsabt, A. M. Ahmed, and F. Ewis, "Recycling rusty iron with natural zeolite heulandite to create a unique nanocatalyst for green hydrogen production," *Nanomaterials*, vol. 11, no. 12, p. 3445, 2021.

[24] N. H. Dahon, M. J. Kassim, N. Nu'Aim Razali, E. M. F. M. Yuslee, A. A. Nasrullah, and N. F. Basri,, "FTIR analysis on phase transformation of rust in the presence of gambir," *Journal of Global Scientific Research*, vol. 1, pp. 54-62, 2018.

[25] M. Jia, P. Hu, and G. Hu, "Corrosion layers on archaeological cast iron from nanhai I," *Materials,* vol. 15, no. 14, p. 4980, 2022.

[26] C. Rémazeilles, and P. Refait, "Fe(II) hydroxycarbonate $Fe_2(OH)_2CO_3$ (chukanovite) as iron corrosion product: Synthesis and study by Fourier Transform Infrared Spectroscopy," *Polyhedron*,vol. 28, no. 4, pp. 749-756, 2009.

[27] K. Wang, Y. Zhuo, J. Chen, D. Gao, Y. Ren, C. Wang, and Z. Qi, "Crystalline phase regulation of anatase-rutile TiO_2 for the enhancement of photocatalytic activity," *RSC Advances*, vol. 10, no. 71, pp. 43592-43598, 2020.

[28] S. Sood, A. Umar, S. K. Mehta, and S. K. Kansal, "Highly effective Fe-doped TiO_2 nanoparticles photocatalysts for visible-light driven photocatalytic degradation of toxic organic compounds," *Journal of Colloid and Interface Science*, vol. 450, pp. 2130-223, 2015.

[29] R. Ebrahimi, A. Maleki, R. Rezaee, H. Daraei, M. Safari, G. Mckay, S-M. Lee, and A. Jafari, "Synthesis and application of Fe-doped TiO_2 nanoparticles for photodegradation of 2,4-D from aqueous solution," *Arabian Journal for Science and Engineering*, vol. 46, no. 7, pp. 6409-6422, 2021.

[30] M. B. Marami, M. Farahmandjou, and B. Khoshnevisan, "Sol–gel synthesis of Fe-doped TiO_2 nanocrystals," *Journal of Electronic Materials*, vol. 47, no. 7, pp. 3741-3748, 2018.

[31] A. F. Shojaei, A. Shams-Nateri, and M. Ghomashpasand, "Magnetically recyclable $Fe^{3+}/TiO_2@Fe_3O_4$ nanocomposites towards degradation of direct blue 71 under visible-light irradiation," *Micro and Nano Letters*, vol. 12, no. 3, pp. 161-165, 2017.

[32] A. Malik, S. Hameed, M. J. Siddiqui, M. M. Haque, and M. Muneer, "Influence of ce doping on the electrical and optical properties of TiO_2 and its photocatalytic activity for the degradation of remazol brilliant blue R," *International Journal of Photoenergy*, vol. 2013, no. 2, p. 1-9, 2013.

[33] W. H. Saputera, A. F. Amri, R. Daiyan, and D. Sasongko, "Photocatalytic technology for palm oil mill effluent (POME) wastewater treatment: Current progress and future perspective," *Materials*, vol. 14, no. 11, p. 2846, 2021.

[34] V. A. R. Villegas, J. D. L. Ramírez, E. H. Guevara, S. P. Sicairos, L. A. H. Ayala, and B. L. Sanchez, "Synthesis and characterization of magnetite nanoparticles for photocatalysis of nitrobenzene," *Journal of Saudi Chemical Society*, vol. 24, no. 2, pp. 223-235, 2020.

[35] Q. Zhang, L. Yu, C. Xu, W. Zhang, M. Chem, Q. Xu, and G. Diao, "A novel method for facile preparation of recoverable $Fe_3O_4@TiO_2$ core-shell nanospheres and their advanced photo-catalytic application," *Chemical Physics Letters*, vol. 761, p. 138073, 2020.

[36] Y. Feng, V. D. Kreslavski, A. N. Shmarev, A. A. Ivanov, S. K. Zharmukhamedov, A. A. Kosobryukhov, M. Yu, S. I. Allakhverdiev, and S. Shabala, "Effects of iron oxide nanoparticles (Fe_3O_4) on growth, photosynthesis, antioxidant activity and distribution of mineral elements in wheat (triticum aestivum) plants," *Plants*, vol. 11, no. 14, p. 1894, 2022.

[37] N. Madima, K. K. Kefeni, S. B. Mishra, A. K. Mishra, and A. T. Kuvarega, "Fabrication of magnetic recoverable Fe_3O_4/TiO_2 heterostructure for photocatalytic degradation of rhodamine B dye.," *Inorganic Chemistry Communications*. vol. 145, no. 1, p. 109966, 2022.

[38] A. C. Chu, R. S. Sahu, T. H. Chou, and Y. H. Shih, "Magnetic $Fe_3O_4@TiO_2$ nanocomposites to degrade bisphenol A, one emerging contaminant, under visible and long wavelength UV light irradiation," *Journal of Environmental Chemical Engineering*, vol. 9, no. 4, p. 105539, 2021.

[39] N. H. Mthombeni, M. S. Onyango, and O. Aoyi, "Adsorption of hexavalent chromium onto magnetic natural zeolite-polymer composite," *Journal of the Taiwan Institute of Chemical Engineers*, vol. 50, pp. 242-251, 2015.

[40] D. Arista, A. Rachmawati, N. Ramadhani, R. E. Saputro, A. Taufiq, and Sunaryono, "Antibacterial performance of Fe_3O_4/PEG-4000 prepared by co-precipitation route," *IOP Conference Series: Materials Science and Engineering*, vol. 515, p. 012085, 2019.

[41] F. Heidarinejad, H. Kamani, and A. Khtibi, "Magnetic Fe-doped TiO_2@Fe_3O_4 for metronidazole degradation in aqueous solutions: Characteristics and efficacy assessment.," *Heliyon*. vol. 9, no. 11, p. e21414, 2023.

[42] X. Yuan, X. Wu, Z. Feng, W. Jia, X. Zheng, and C. Li, "Facile synthesis of heterojunctioned ZnO/Bi_2S_3 nanocomposites for enhanced photocatalytic reduction of aqueous Cr(Vi) under visible-light irradiation," *Catalysts*, vol. 9, no. 7, pp. 1-14, 2019.

[43] J. Preethi, M. H. Farzana, and S. Meenakshi, "Photo-reduction of Cr(VI) using chitosan supported zinc oxide materials," *International Journal of Biological Macromolecules,* vol. 104, no. Part B, pp. 1783-1793, 2017.

[44] B. Zhao, H. Xu, K. Zhang, B. Gao, Y. Wang, Q. Wang, K. Zhang, Y. Huang, and J. Ii, "Visible-light-driven CQDs/TiO_2 photocatalytic simultaneous removal of Cr(VI) and organics: Cooperative reaction, kinetics and mechanism," *Chemosphere*, vol. 307, no. Part 2, p. 135897, 2022.

[45] A. Prastika, and I. Alamsah, "Kinetika adsorpsi asam tanat pada fotokatalis SiO_2/TiO_2," *Jurnal teknologi terapan*, vol. 06, no. 1, pp. 14-22, 2022.

[46] Y. Yuniar, E. T. Wahyuni, and N. H. Aprilita, "Photoreduction of Cr(VI) Catalyzed by TiO_2-Lignin.," *Indonesian Journal of Fundamental and Applied Chemistry*. vol. 2, no. 1, pp. 22-27, 2017.

47] R. Djellabi, P. Su, A. Elimian, V. Poliukhova, S. Nouacer, I. A. Abdelhafeez, N. Abderrahim, D. Aboagye, V. Andhalkar, W. Nabgan, S. Rtimi, and S. Contreras, "Advances in photo-catalytic reduction of hexavalent chromium: From fundamental concepts to materials design and technology challenges," *Journal of Water Process Engineering*, vol. 50, p. 103301, 2022.